

## Quasinormal Modes of Black Holes with Multiple Photon Spheres

Guangzhou Guo<sup>a,\*</sup>, Peng Wang<sup>a,†</sup>, Houwen Wu<sup>a,b,‡</sup> and Haitang Yang<sup>a,§</sup>

<sup>a</sup>*Center for Theoretical Physics, College of Physics,  
Sichuan University, Chengdu, 610064, China and*

<sup>b</sup>*Department of Applied Mathematics and Theoretical Physics,  
University of Cambridge, Wilberforce Road, Cambridge, CB3 0WA, UK*

For a static and spherically symmetric black hole, a photon sphere is composed of circular null geodesics of fixed radius, and plays an important role in observing the black hole. Recently, in an Einstein-Maxwell-scalar model with a non-minimal coupling between the scalar and electromagnetic fields, a class of hairy black holes has been found to possess two unstable and one stable circular null geodesics on the equatorial plane, corresponding to three photon spheres outside the event horizon. In this paper, we study quasinormal modes of the scalar field, which are associated with these circular null geodesics, in the hairy black hole spacetime. In the eikonal regime with  $l \gg 1$ , the real part of the quasinormal modes is determined by the angular velocity of the corresponding circular geodesics. The imaginary part of the quasinormal modes associated with the unstable circular null geodesics encodes the information about the Lyapunov exponent of the corresponding circular geodesics. Interestingly, we find long-lived and sub-long-lived modes, which are associated with the stable and one of the unstable circular null geodesics, respectively. Due to tunneling through potential barriers, the damping times of the long-lived and sub-long-lived modes can be exponentially and logarithmically large in terms of  $l$ , respectively.

---

\* [gzguo@stu.scu.edu.cn](mailto:gzguo@stu.scu.edu.cn)

† [pengw@scu.edu.cn](mailto:pengw@scu.edu.cn)

‡ [hw598@damtp.cam.ac.uk](mailto:hw598@damtp.cam.ac.uk)

§ [hyanga@scu.edu.cn](mailto:hyanga@scu.edu.cn)

## CONTENTS

I. Introduction	2
II. Hairy Black Holes	4
A. Black Hole Solution	4
B. Circular Null Geodesics	5
C. Lyapunov Exponent	6
III. Quasinormal Modes	8
A. Modes at Global Maximum	10
B. Long-lived Modes at Minimum	11
C. Sub-long-lived Modes at Local Maximum	14
IV. Conclusions	18
Acknowledgments	19
A. Derivations of Eqns. (34) and (36)	19
References	20

## I. INTRODUCTION

In the last decade, gravitational waves from a binary black hole merger were successfully detected by LIGO and Virgo [1], and subsequently the first image of a supermassive black hole at the center of galaxy M87 was photographed by the Event Horizon Telescope (EHT) [2–7], which opens a new era of black hole physics. Due to the event horizon, a black hole is a dissipative system, eigenmodes of which are quasinormal modes. The final stage of a binary black hole merger is ringdown, in which the gravitational waveforms are described by a superposition of quasinormal modes [8]. Quasinormal modes with complex frequencies have vast applications in black hole physics [9–20]. In particular, a linear perturbation can induce a discrete set of quasinormal modes, whose imaginary part is related to the damping time scale. The spectrum of quasinormal modes therefore provides a perspective on the study of stability of the background spacetime [21–26]. Moreover, the most dominant quasinormal modes can be used to check the validity of the strong cosmic censorship conjecture [27–29].

Since exotic horizonless objects, e.g., wormholes and ultra-compact objects (UCOs), have optical observations similar to black holes, they have recently attracted great attention [30–37]. Interestingly, a reflecting boundary in the wormhole or UCO spacetime can produce a set of time-delay echoes, which are characterized by quasinormal modes [38–41]. Furthermore, UCOs have been conjectured to suffer from instabilities due to the existence of a family of long-lived quasinormal modes, which appear in the neighborhood of a stable circular null geodesic [42–44]. For instance, a linear ergoregion instability associated with long-lived modes may occur for a spinning object with a sufficiently high rotation speed [45–47].

Intriguingly, unstable null geodesics have been revealed to be closely related to a class of quasinormal modes of perturbations in the black hole spacetime [9, 10, 16, 48–52]. In [9], null geodesics were first found to be connected with quasinormal modes in Schwarzschild and slowly rotating Kerr black holes. Using the WKB approximation in the eikonal limit, the authors of [48] elaborated the connection in the static, spherically symmetric and asymptotically flat black hole background. To be more specific, it verified that the real part of quasinormal modes is proportional to the angular velocity of the corresponding unstable circular null geodesic, while the imaginary part is determined by the Lyapunov exponent of the orbit. Furthermore, the relation between null geodesics and quasinormal modes was generalized to Kerr black holes of arbitrary spin in [16], which showed an extra precession modification in the real part compared to non-rotating black holes.

The No-hair theorem asserts that a black hole is uniquely determined by its three parameters, i.e., mass, electric charge and angular momentum [53–55]. However, hairy black holes with extra freedom have been constructed in various models, which provide counter-examples to the no-hair theorem [56–62]. Recently, a type of Einstein-Maxwell-scalar (EMS) models with a non-minimal coupling between the scalar and electromagnetic fields have been extensively studied in the literature [23, 26, 63–78]. In the EMS models, the non-minimal coupling destabilizes scalar-free black holes and induce the onset of spontaneous scalarization to form hairy black holes with a scalar hair [63]. In [24, 25, 79], the stability of the hairy black holes was analyzed by calculating their quasinormal modes of various perturbations. Decaying quasinormal modes may suggest that the hairy black holes are the endpoints of the dynamic evolution from unstable scalar-free black hole solutions.

Surprisingly, it showed that in a certain parameter regime of the hairy black holes, there exist two unstable and one stable null circular null geodesics on the equatorial plane, which indicates three photon spheres of different sizes outside the event horizon [76, 77]. Due to a double-peak structure appearing in the potential of the photon radial motion, the existence of two unstable

photon spheres can remarkably affect the optical appearance of black holes illuminated by the surrounding accretion disk, e.g., leading to bright rings of different radii in the black hole image [76] and significantly increasing the flux of the observed image [77]. The relation between null geodesics and quasinormal modes has been rarely reported for black holes with more than one photon sphere. Moreover, multiple photon spheres appearing in some spacetime signal the existence of long-live modes, which may render the spacetime unstable [42–44]. Therefore, it is of great interest to study quasinormal modes of the hairy black holes endowed with three photon spheres. Note that multiple photon spheres have recently been reported in different black hole models [80–82].

In this paper, we use the WKB method to calculate quasinormal modes localized at circular null geodesics of the hairy black holes with three photon spheres. The rest of the paper is organized as follows. In Section II, we study null circular geodesics of hairy black holes in the EMS model, as well as the orbital stability by evaluating the Lyapunov exponent. Subsequently, quasinormal modes trapped at different circular null geodesics are obtained in Section III. We conclude our main results in Section IV. The Appendix A is devoted to derivations of some WKB formulas. We set  $16\pi G = 1$  throughout this paper.

## II. HAIRY BLACK HOLES

In this section, we first briefly review spherically symmetric hairy black hole solutions in the EMS model. Subsequently, we study circular geodesics for photons around the hairy black holes and compute the corresponding Lyapunov exponents.

### A. Black Hole Solution

In the EMS model, the action is given by

$$S = \int d^4x \sqrt{-g} \left[ R - 2\partial_\mu \phi \partial^\mu \phi - e^{\alpha\phi^2} F^{\mu\nu} F_{\mu\nu} \right], \quad (1)$$

where the scalar field  $\phi$  is minimally coupled to the metric field and non-minimally coupled to the electromagnetic field  $A_\mu$ . Here,  $F_{\mu\nu} = \partial_\mu A_\nu - \partial_\nu A_\mu$  is the electromagnetic field strength tensor, and  $e^{\alpha\phi^2}$  is the coupling function between  $\phi$  and  $A_\mu$ . Following [26, 63], we restrict our attention to static, spherically symmetric and asymptotically flat black hole solutions with the generic ansatz

$$ds^2 = -N(r) e^{-2\delta(r)} dt^2 + \frac{1}{N(r)} dr^2 + r^2 (d\theta^2 + \sin^2 \theta d\varphi^2),$$

$$A_\mu dx^\mu = V(r) dt \text{ and } \phi = \phi(r). \quad (2)$$

The equations of motion are then given by

$$\begin{aligned}
N'(r) &= \frac{1 - N(r)}{r} - \frac{Q^2}{r^3 e^{\alpha\phi^2(r)}} - rN(r)\phi'^2(r), \\
[r^2 N(r)\phi'(r)]' &= -\frac{\alpha\phi(r)Q^2}{e^{\alpha\phi^2(r)}r^2} - r^3 N(r)\phi'^3(r), \\
\delta'(r) &= -r\phi'^2(r), \\
V'(r) &= \frac{Q}{r^2 e^{\alpha\phi^2(r)}} e^{-\delta(r)},
\end{aligned} \tag{3}$$

where primes denote derivatives with respect to  $r$ , and the integration constant  $Q$  is interpreted as the electric charge of the black hole solution.

To find black holes solutions from the non-linear ordinary differential equations (3), one needs to impose proper boundary conditions at the event horizon  $r_h$  and the spatial infinity,

$$\begin{aligned}
N(r_h) &= 0, \quad \delta(r_h) = \delta_0, \quad \phi(r_h) = \phi_0, \quad V(r_h) = 0, \\
N(\infty) &= 1, \quad \delta(\infty) = 0, \quad \phi(\infty) = 0, \quad V(\infty) = \Phi,
\end{aligned} \tag{4}$$

where  $\Phi$  is the electrostatic potential. The two parameters  $\delta_0$  and  $\phi_0$  determine the asymptotic behavior of the solutions in the vicinity of the horizon. Moreover, the black hole mass  $M$ , which is related to the ADM mass, can be obtained via  $M = \lim_{r \rightarrow \infty} r[1 - N(r)]/2$ . In this paper, we set  $M = 1$  and use a shooting method to numerically solve eqn. (3) for black hole solutions matching the boundary conditions (4). It is manifest that the scalar-free solutions with  $\phi = 0$  (i.e., Reissner-Nordström black holes) can exist in the EMS model. Nevertheless, we focus on hairy black holes with the non-trivial profile of the scalar field  $\phi$ . For instance, we exhibit the profile of the metric functions for the hairy black hole solution with  $\alpha = 0.9$  and  $Q = 1.066$  in the left panel of FIG. 1.

## B. Circular Null Geodesics

Owing to strong gravity near a black hole, photons are forced to travel in circular null geodesics on photon spheres, which play an important role in determining properties of the black hole image seen by a distant observer (e.g., the size of the black hole shadow). Here, circular null geodesics of the spherically symmetric hairy black hole are studied. Without loss of generality, we consider a photon moving on the equatorial plane with  $\theta = \pi/2$ . To obtain equatorial geodesics, we start from the Lagrangian

$$\mathcal{L} = \frac{1}{2} \left( -N(r) e^{-2\delta(r)} \dot{t}^2 + \frac{1}{N(r)} \dot{r}^2 + r^2 \dot{\phi}^2 \right), \tag{5}$$

where dots denote derivatives with respect to the affine parameter  $\tau$ . The generalized canonical momenta for this Lagrangian are defined as

$$\begin{aligned} -p_t &= N(r) e^{-2\delta(r)} \dot{t} = E, \\ p_\varphi &= r^2 \dot{\varphi} = L, \\ p_r &= \frac{1}{N} \dot{r}. \end{aligned} \tag{6}$$

Note that the metric of the hairy black hole spacetime is independent of  $t$  and  $\varphi$ . So the spacetime admits two Killing vectors, which are associated with the conserved energy  $E$  and momentum  $L$ , respectively, in eqn. (6). Varying the Lagrangian (5) with respect to  $r$  yields the radial equation of motion for the photon,

$$\frac{d}{d\tau} \frac{\partial \mathcal{L}}{\partial \dot{r}} = \frac{\partial \mathcal{L}}{\partial r}. \tag{7}$$

With the help of eqn. (6), eqn. (7) becomes

$$e^{-2\delta(r)} \dot{r}^2 = E^2 - \frac{e^{-2\delta(r)} N(r)}{r^2} L^2, \tag{8}$$

which describes a null geodesic. For later use, one can introduce the geometric potential as

$$V_{\text{geo}}(r) = \frac{e^{-2\delta(r)} N(r)}{r^2}. \tag{9}$$

Accordingly, a null circular geodesic at  $r = r_c$  can appear, provided that the conditions  $V_{\text{geo}}(r_c) = E^2/L^2$  and  $V'_{\text{geo}}(r_c) = 0$  are satisfied.

In FIG. 1, we present the geometric potential for hairy black holes with  $\alpha = 0.9$  for  $Q = 1.066$ , 1.064 and 1.059 in the right panel. When  $Q = 1.059$  (the blue line), the geometric potential possesses a single maximum outside the event horizon. Intriguingly for  $Q = 1.066$  and 1.064 (the red and orange lines), it displays a double-peak structure with one minimum and two maxima, which implies that there exist three null circular geodesics located at the extrema.

### C. Lyapunov Exponent

The Lyapunov exponent is proposed to characterize the rate of separation of adjacent trajectories in the phase space [48, 83]. In a dynamical system, the sign of the Lyapunov exponent can be used to determine whether adjacent trajectories converge or not. Specifically, positive Lyapunov exponents correspond to the divergent trajectories, while negative ones to the convergent trajectories. Therefore, we can study the stability of null circular orbits around a hairy black hole by

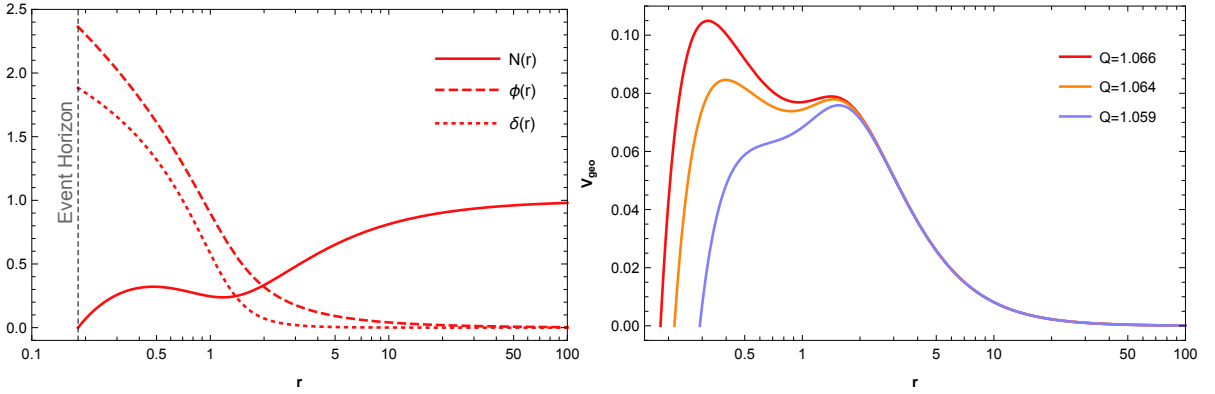


FIG. 1. Metric functions and geometric potential for hairy black hole solutions, where we take  $\alpha = 0.9$ . **Left:** The metric functions  $N(r)$  (solid line),  $\phi(r)$  (dashed line) and  $\delta(r)$  (dotted line) for the hairy black hole solution with  $Q = 1.066$  are plotted outside the event horizon (vertical dashed line). **Right:** The geometric potential for different hairy black holes with  $Q = 1.066$  (red line),  $Q = 1.064$  (orange line) and  $Q = 1.059$  (blue line). For a large value of charge (e.g., the red and orange lines), the geometric potential possesses a double-peak structure with one local minimum and two local maxima. By contrast, the double-structure disappears as the charge decreases (e.g., the blue line), leaving only a single maximum of the geometric potential.

evaluating their Lyapunov exponents. Moreover, the Lyapunov exponent can be closely related to quasinormal modes of black holes. Indeed, it showed in [48] that, if the geometric potential has a single maximum, the imaginary part of quasinormal modes is determined by the Lyapunov exponent of the unstable circular orbit at the maximum in the eikonal regime.

To describe circular orbits in spherically symmetric spacetime, we focus on a two dimensional phase space spanned by  $X_i(t) \equiv (p_r, r)$ . The equations of motion in this phase space can be schematically written as

$$\frac{dX_i}{dt} = H_i(X_j). \quad (10)$$

To obtain the Lyapunov exponent of a given orbit, we need to linearize eqn. (10) around the orbit,

$$\frac{d\delta X_i(t)}{dt} = K_{ij}(t) \delta X_j(t), \quad (11)$$

where the linear stability matrix  $K_{ij}(t)$  is

$$K_{ij}(t) = \left. \frac{\partial H_i}{\partial X_j} \right|_{X_i(t)} = \begin{pmatrix} 0 & d(\dot{t}^{-1} p_r) / dr \\ \dot{t}^{-1} N & 0 \end{pmatrix}. \quad (12)$$

The solution to the linearized equation (11) can be expressed as

$$\delta X_i(t) = L_{ij}(t) \delta X_j(0), \quad (13)$$

where the evolution matrix  $L_{ij}(t)$  satisfies

$$\frac{dL_{ij}(t)}{dt} = K_{im}(t) L_{mj}(t), \quad (14)$$

and  $L_{ij}(0) = \delta_{ij}$ . The principal Lyapunov exponent is related to the determination of the eigenvalues of  $L_{ij}$ , i.e.,

$$\lambda = \lim_{t \rightarrow \infty} \frac{1}{t} \log \frac{L_{jj}(t)}{L_{jj}(0)}. \quad (15)$$

From eqn. (12), the principal Lyapunov exponent can be written as

$$\lambda = \pm \sqrt{t^{-1} N \frac{d}{dr} (t^{-1} \dot{p}_r)}, \quad (16)$$

where we choose the + sign for the Lyapunov exponent [48]. Specifically, the Lyapunov exponent of a circular orbit at  $r = r_c$  can be expressed in terms of the geometric potential,

$$\lambda|_{r=r_c} = \sqrt{-\frac{L^2 e^{2\delta}}{2t^2} V''_{\text{geo}}}\bigg|_{r=r_c} = \sqrt{-\frac{1}{2V_{\text{geo}}} \frac{d^2}{dx^2} V_{\text{geo}}}\bigg|_{r=r_c}, \quad (17)$$

where the tortoise coordinate  $x$  is defined by  $dx/dr \equiv e^{\delta(r)} N^{-1}(r)$ . For a circular null orbit located at a local maximum of the geometric potential with  $V''_{\text{geo}} < 0$ , the Lyapunov exponent  $\lambda$  is positive, which implies that the orbit is unstable under small perturbations. On the other hand, a circular orbit located at a local minimum has  $V''_{\text{geo}} < 0$  and hence has a purely imaginary value of the Lyapunov exponent, which implies that the orbit is stable. Therefore, a black hole with a double-peak geometric potential (e.g.,  $Q = 1.066$  and  $1.064$  in FIG. 1) has two unstable circular null geodesics at the local maxima and a stable one at the local minimum. In addition, we introduce the angular velocity  $\Omega$  of the circular orbit at  $r = r_c$  via

$$\Omega|_{r=r_c} = \frac{\dot{\varphi}}{t}\bigg|_{r=r_c} = \sqrt{V_{\text{geo}}}\bigg|_{r=r_c}, \quad (18)$$

which can be related to the real part of quasinormal modes [48].

### III. QUASINORMAL MODES

In this section, we consider the perturbation of the scalar field and compute its quasinormal modes that are associated with the circular null geodesics in the hairy black hole background (2).

For a scalar perturbation of mode

$$\delta\phi = e^{-i\omega t} \frac{\Psi_{\omega l}(r) Y_{lm}(\theta, \phi)}{r}, \quad (19)$$

we can separate the angular variables and express the linearized equation for  $\Psi_{\omega l}(r)$  in the following general form,

$$\left( \frac{d^2}{dx^2} + \omega^2 - V_l(r) \right) \Psi_{\omega l}(r) = 0, \quad (20)$$

where the effective potential is

$$V_l(r) = \frac{e^{-2\delta(r)} N(r)}{r^2} \left[ l(l+1) + 1 - N(r) - \frac{Q^2}{r^2 e^{\alpha\phi(r)^2}} - \left( \alpha + 2\alpha^2\phi(r)^2 \right) \frac{Q^2}{r^2 e^{\alpha\phi(r)^2}} \right]. \quad (21)$$

In the eikonal regime ( $l \gg 1$ ), the effective potential reduces to

$$V_l(r) \simeq l^2 \frac{e^{-2\delta(r)} N(r)}{r^2} = l^2 V_{\text{geo}}(r), \quad (22)$$

where  $V_{\text{geo}}(r)$  is the aforementioned geometric potential. It is worth emphasizing that the full perturbed fields around the hairy black hole background were considered in [24]. In the eikonal limit, the scalar perturbation decouples with other perturbations, and the scalar perturbative equation then reduces to eqn. (20) with the effective potential (22).

In FIG. 2, we plot the effective potential  $V_l$  with  $l = 3$  for the hairy black hole solution with  $\alpha = 0.9$  and  $Q = 1.066$ . Like the geometric potential,  $V_l$  displays a double-peak structure, i.e., two local maxima and one minimum. The effective potential  $V_l$  with  $l > 3$  is found to have a similar profile. Since quasinormal modes are determined by the effective potential  $V_l$ , multiple local extrema of  $V_l$  could lead to distinct types of quasinormal modes. In the rest of the section, we apply the WKB approximation to studying quasinormal modes trapped at the extrema of the effective potential with a double-peak structure. These modes can be interpreted as photons moving in the circular null geodesics determined by  $V_{\text{geo}}(r)$ , which leak out slowly. Since we are interested in the large  $l$  limit, the WKB approximation can be accurate enough for computing quasinormal modes. For comparison, we perform a direct integration to numerically solve eqn. (20) to obtain the exact quasinormal modes of interest for the hairy black hole with  $\alpha = 0.9$  and  $Q = 1.066$ . Note that quasinormal modes occur only when appropriate boundary conditions are imposed, i.e., purely ingoing modes at  $x = -\infty$  (at the event horizon) and purely outgoing modes at  $x = +\infty$  (at the spatial infinity). Without causing any ambiguity, we denote the geometric potential, the effective potential and the metric functions with respect to the tortoise coordinate  $x$  by  $V_{\text{geo}}(x)$ ,  $V_l(x)$ ,  $N(x)$  and  $\delta(x)$ , respectively.

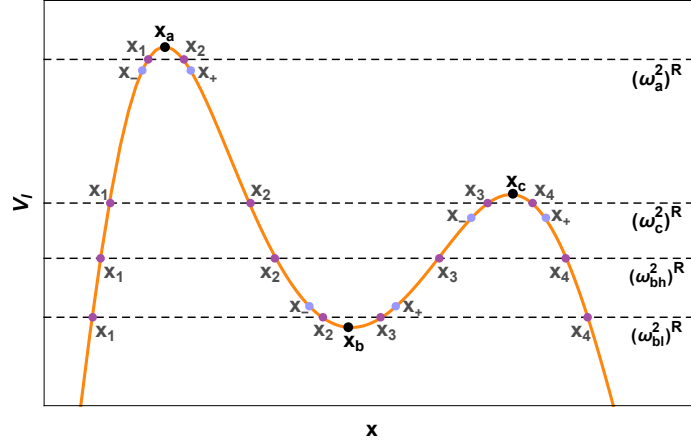


FIG. 2. The effective potential  $V_l$  as a function of the tortoise coordinate  $x$ . Here we present a local region of the effective potential for the hairy black hole with  $\alpha = 0.9$  and  $Q = 1.066$ . Note that the effective potential tends to vanish as  $x \rightarrow \pm\infty$ . The horizontal dashed lines represent the real parts of quasinormal modes  $\omega^2$  in different cases, which intersect the effective potential at the turning points labelled by  $x_1, x_2, x_3$  and  $x_4$ . The black points denote the extrema of  $V_l$  at  $x_a, x_b$  and  $x_c$ , respectively, which correspond to the circular null geodesics in the eikonal limit. Around the extrema, the effective potential can be approximated by a parabola between the blue points  $x_-$  and  $x_+$ .

### A. Modes at Global Maximum

We first discuss the quasinormal modes of frequency  $\omega_a$  trapped at the global maximum of the effective potential at  $x = x_a$ . For such modes, the  $(\omega_a^2)^R$  line lies close to the global maximum and intersects the potential at the turning points  $x_1$  and  $x_2$ , around which the WKB approximation fails. There exists some small positive constant  $\delta$  such that the WKB approximation is valid for  $x < x_1 - \delta$  and  $x > x_2 + \delta$ . Therefore, the solution of eqn. (20) can be approximated by the WKB expansions in  $(-\infty, x_1 - \delta)$  and  $(x_2 + \delta, +\infty)$ , which match the ingoing and outgoing boundary conditions, respectively. In the vicinity of  $x = x_a$ , the potential can be approximated by a parabola. If  $(\omega_a^2)^R$  is close enough to the global maximum, there exist  $x_-$  and  $x_+$  with  $x_- < x_1 - \delta < x_2 + \delta < x_+$ , such that the effective potential is well approximated by a parabola for  $x_- < x < x_+$  (see FIG. 2). In  $(x_-, x_+)$ , eqn. (20) with an approximated parabolic potential can be exactly solved in terms of parabolic cylinder functions. Furthermore, a complete solution requires that the two WKB expansions should be smoothly connected by the exact solution in the overlapping regions  $(x_-, x_1 - \delta)$  and  $(x_2 + \delta, x_+)$ . The matching procedure then gives [84]

$$\frac{\omega_a^2 - V_l(x_a)}{\sqrt{-2V_l^{(2)}(x_a)}} = i \left( n + \frac{1}{2} \right) \quad \text{with } n = 0, 1, 2, \dots, \quad (23)$$

where the superscript of  $V_l^{(2)}(x_a)$  denotes the second derivative over the tortoise coordinate  $x$ .

The matching condition (23) leads to a set of discrete quasinormal modes  $\omega_a$ , labelled by the integer  $n$ . In the eikonal regime ( $l \gg 1$ ), the quasinormal modes reduce to

$$\omega_a = l\sqrt{V_{\text{geo}}(x_a)} - i\left(n + \frac{1}{2}\right)\sqrt{-\frac{V_{\text{geo}}^{(2)}(x_a)}{2V_{\text{geo}}(x_a)}}, \quad (24)$$

where  $x_a$  becomes the global maximum of the geometric potential in the eikonal limit. Using eqns. (17) and (18), one can express the quasinormal modes (24) as

$$\omega_a = \Omega_a l - i\left(n + \frac{1}{2}\right)\lambda_a, \quad (25)$$

where  $\Omega_a$  and  $\lambda_a$  are the angular velocity and the Lyapunov exponent of the unstable circular orbit at the global maximum of the geometric potential, respectively. Interestingly, since the Lyapunov exponent of the unstable circular orbit describes the instability timescale of the geodesic motion, the Lyapunov exponent contributes to the imaginary part of the quasinormal modes. Note that the case with a single maximum of the geometric potential was found to have the same relation between quasinormal modes and circular null geodesics as eqn. (25) [48].

## B. Long-lived Modes at Minimum

In this subsection, the quasinormal modes of low and high excitations trapped at the minimum of the effective potential are derived via the WKB approximation, respectively. We find that there exist long-lived quasinormal modes, which is related to the stable circular null geodesic with a purely imaginary Lyapunov exponent. It is noteworthy that the existence of long-lived modes has been reported in the spacetime of ECOs with an unstable photon orbit [42].

We first discuss the low-lying quasinormal modes of frequency  $\omega_{bl}$ . As illustrated in FIG. 2, the  $(\omega_{bl}^2)^R$  line intersects the effective potential at the turning points  $x_1, x_2, x_3$  and  $x_4$ . Suppose the WKB approximation is valid at a distance  $\delta$  away from these turning points, where  $\delta > 0$  is a small constant. If the  $(\omega_{bl}^2)^R$  line is close enough to the local minimum at  $x = x_b$ , both  $x_2 - \delta$  and  $x_3 + \delta$  can lie in the interval  $(x_-, x_+)$ , in which the effective potential is well approximated by a parabolic expansion. With the approximated parabolic potential, the exact solution of eqn. (20) can be expressed in terms of parabolic cylinder functions for  $x \in (x_-, x_+)$ . In addition, the effective potential can be approximated by a linear function near  $x_1$  and  $x_4$ , which leads to the exact solutions in the neighborhoods of  $x_1$  and  $x_4$ . The WKB expansions are required to match the exact solution in  $(x_-, x_2 - \delta)$ ,  $(x_3 + \delta, x_+)$  and the neighborhoods of  $x_1$  and  $x_4$ . This matching

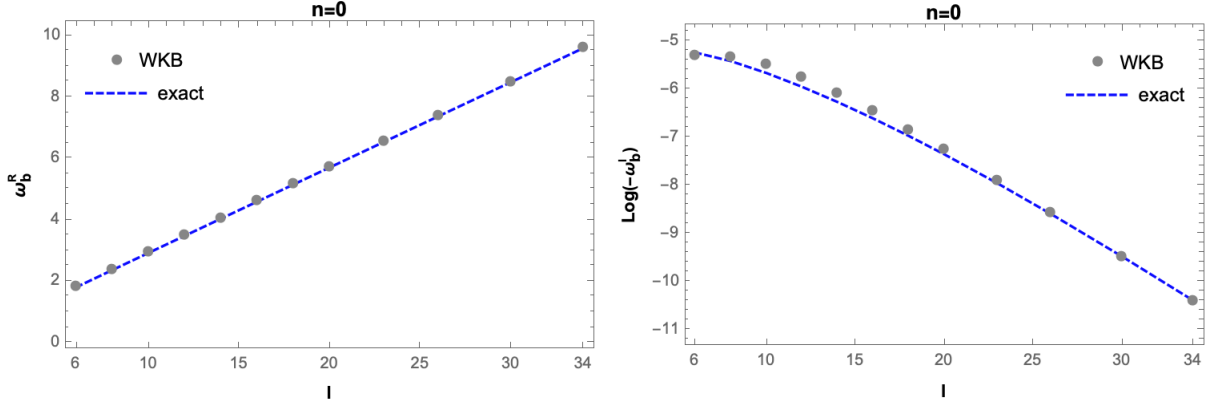


FIG. 3. Real (**Left**) and imaginary (**Right**) parts of the lowest-lying quasinormal modes ( $n = 0$ ) trapped at the stable circular null geodesic. Blue dashed lines represent the exact modes obtained by a numerical method of direct integration, while gray dots denote the WKB results. The real part  $\omega_b^R$  increases monotonically with  $l$ . For a large  $l$ , the ratio between  $\omega_b^R$  and  $l$  is the angular velocity of the circular geodesic. The magnitude of  $\omega_b^I$  decreases exponentially as  $l$  increases, which indicates a class of long-lived modes.

strategy then gives a family of quasinormal modes [85],

$$\begin{aligned} (\omega_{bl}^2)^R &= V_l(x_b) + \left(n + \frac{1}{2}\right) \sqrt{2V_l^{(2)}(x_b)}, \\ (\omega_{bl}^2)^I &= -\frac{\gamma_n^2}{2 \int_{x_2}^{x_3} \frac{dx}{\sqrt{(\omega_{bl}^R)^2 - V_l(x)}}} \left( e^{-2 \int_{x_1}^{x_2} \sqrt{V_l(x) - (\omega_{bl}^R)^2} dx} + e^{-2 \int_{x_3}^{x_4} \sqrt{V_l(x) - (\omega_{bl}^R)^2} dx} \right), \end{aligned} \quad (26)$$

where

$$\gamma_n = \pi^{1/4} \frac{1}{2^{n/2} \sqrt{n!}} \left( \frac{2n+1}{e} \right)^{\frac{1}{2}(n+\frac{1}{2})}. \quad (27)$$

Moreover, eqn. (26) indicates  $(\omega_{bl}^2)^R - V_l(x_b) \propto n + \frac{1}{2}$ , which means that a large  $n$  can drive the  $(\omega_{bl}^2)^R$  line away from the local minimum, making  $x_2 \in (x_-, x_+)$  and  $x_3 \in (x_-, x_+)$  impossible. Therefore, eqn. (26) is only applicable to the low-lying modes with small  $n$ . In FIG. 3, eqns. (26) is used to evaluate the lowest-lying modes ( $n = 0$ ) of the hairy black hole with  $\alpha = 0.9$  and  $Q = 1.066$ , which are denoted by gray dots. Additionally, a direct integration numerically solves eqn. (20) for exact modes, which are represented by blue dashed lines. We plot the real part  $\omega_{bl}^R$  against  $l$  in the left panel, which shows that the WKB results match well with the numerical ones. As for the imaginary part  $\omega_b^I$  in the right panel, the WKB results differ a little from the numerical ones for a small  $l$ . Nevertheless, the WKB results tend to approach the numerical ones as  $l$  increases, which demonstrates that the WKB approximation is accurate enough when  $l$  is large enough.

In the large  $l$  limit, the real part  $\omega_{bl}^R$  can be approximated by,

$$\omega_{bl}^R \sim \Omega_b l - i \left( n + \frac{1}{2} \right) \lambda_b \sim \Omega_b l, \quad l \gg 1, \quad (28)$$

where  $\Omega_b$  is the angular velocity of the stable circular orbit at  $x = x_b$ , and  $\lambda_b$  is the corresponding Lyapunov exponent. Unlike the global maximum case, the Lyapunov exponent  $\lambda_b$  is purely imaginary for the stable circular null geodesic, and hence contributes to the real part of quasinormal modes. Nevertheless, the correction to  $\omega_{bl}^R$  due to  $\lambda_b$  is negligible for a small value of  $n$  in the large  $l$  limit. Hence, the real part of the low-lying quasinormal modes trapped at the stable circular orbit is proportional to the corresponding angular velocity. Schematically in the eikonal limit, the imaginary part  $\omega_{bl}^I$  can be expressed as

$$\omega_{bl}^I \sim -d \left( e^{-c_1 l} + e^{-c_2 l} \right), \quad l \gg 1, \quad (29)$$

where  $d$ ,  $c_1$  and  $c_2$  are positive constants. It is observed that  $\omega_{bl}^I$  decays exponentially with respect to  $l$  due to the double potential barriers. In fact,  $\omega_{bl}^I$  is related to the flux density of leaking modes outside the double potential barriers. An exponentially small value of  $\omega_{bl}^I$  indicates that the double potential barriers trap these modes in the potential valley with an exponentially large damping time. The quasinormal modes living in the vicinity of the stable null geodesic are thus dubbed as the long-lived modes. Since the long-lived modes can accumulate around the stable null geodesic, their backreaction onto spacetime may render the hairy black holes with a double-peak structure unstable [42–44].

To study quasinormal modes at high excitation ( $n \gg 1$ ), we consider the  $(\omega_{bh}^2)^R$  line at some distance away from the local minimum, which is illustrated in FIG. 2. In the vicinity of each turning point, the effective potential can be approximated by a linear function. Then in the neighborhoods of the turning points, eqn. (20) can be exactly solved in terms of Airy functions. Away from the turning points, WKB solutions provide a good approximation. To obtain a complete solution, the WKB solutions should be smoothly glued up by the exact solutions near the turning points, which leads to the generalized Born-Sommerfeld quantization rule [85, 86],

$$\int_{x_2}^{x_3} \sqrt{\omega_{bh}^2 - V_l(x)} dx - \frac{i}{4} \left( e^{-2 \int_{x_1}^{x_2} \sqrt{V_l(x) - \omega_{bh}^2} dx} + e^{-2 \int_{x_3}^{x_4} \sqrt{V_l(x) - \omega_{bh}^2} dx} \right) = \pi \left( n + \frac{1}{2} \right). \quad (30)$$

In the large  $l$  limit, we extract the real part of quasinormal modes from the quantization rule (30), which reads

$$\int_{x_2}^{x_3} \sqrt{(\omega_{bh}^R)^2 - V_l(x)} dx = \pi \left( n + \frac{1}{2} \right). \quad (31)$$

After the real part  $\omega_{bh}^R$  is obtained, the imaginary part  $\omega_{bh}^I$  is then given by

$$\omega_{bh}^I = -\frac{1}{4\omega_{bh}^R \int_{x_2}^{x_3} \frac{\sigma(x)}{\sqrt{(\omega_{bh}^R)^2 - V_l(x)}} dx} \left( e^{-2 \int_{x_1}^{x_2} \sqrt{V_l(x) - (\omega_{bh}^R)^2} dx} + e^{-2 \int_{x_3}^{x_4} \sqrt{V_l(x) - (\omega_{bh}^R)^2} dx} \right), \quad (32)$$

where

$$\sigma(x) = 2 \cos^2 \left( -\frac{\pi}{4} + \int_{x_2}^x \sqrt{(\omega_{bh}^R)^2 - V_l(x)} dx \right). \quad (33)$$

Since the  $(\omega_{bh}^2)^R$  line is not close to the local minimum, the left-hand side of eqn. (31) becomes large in the eikonal limit, leading to a large  $n$ . Thus, eqns. (31) and (32) describe the quasinormal modes at high excitation with  $n \gg 1$ . In this case,  $\sigma(x)$  oscillates dramatically between  $x_2$  and  $x_3$ , and hence one has  $\sigma(x) \approx 1$  under the integration of eqn. (32). Consequently, the imaginary part of high excitation modes (32) can also be schematically written as eqn. (29) in the eikonal limit. So for  $l \gg 1$ , the quasinormal modes at high excitation are also long-lived modes.

### C. Sub-long-lived Modes at Local Maximum

Finally, the quasinormal modes of frequency  $\omega_c$ , which live near the smaller local maximum (i.e., the local maximum smaller than the global maximum), are investigated. As illustrated in FIG. 2, we consider the  $(\omega_c^2)^R$  line lying in the vicinity of the local maximum at  $x = x_c$ , which is associated with the outer unstable circular null geodesic. Following the analogous strategy as before, the effective potential is approximated with a parabola in the interval  $(x_-, x_+)$ , and a linear function near the turning points  $x_1$  and  $x_2$ . In addition, the turning points  $x_3$  and  $x_4$  are assumed to lie in  $(x_-, x_+)$ , which means that the WKB expansions near  $x_3$  and  $x_4$  can match the exact solution with the parabolic potential. Considering the boundary conditions and matching the WKB expansions with the exact solutions near the turning points, we find the frequency of the quasinormal modes is determined by (see Appendix A for the derivation)

$$\int_{x_2}^{x_3} \sqrt{\omega_c^2 - V_l(x)} dx + \xi + \frac{i}{4} e^{-2 \int_{x_1}^{x_2} \sqrt{V_l(x) - \omega_c^2} dx} = \left( n + \frac{1}{4} \right) \pi, \quad (34)$$

where  $\xi$  is defined by

$$e^{-2i\xi} = e^{-i\pi\nu + (\nu+1/2)} \left( \nu + \frac{1}{2} \right)^{-(\nu+1/2)} \frac{\sqrt{2\pi}}{\Gamma(-\nu)}, \quad \nu + \frac{1}{2} = i \frac{\omega_c^2 - V_l(x_c)}{\sqrt{-2V_l^{(2)}(x_c)}}. \quad (35)$$

Roughly speaking, the trapping in the potential valley and the tunneling through the left potential barrier result in the first and last terms of eqn. (34), respectively.

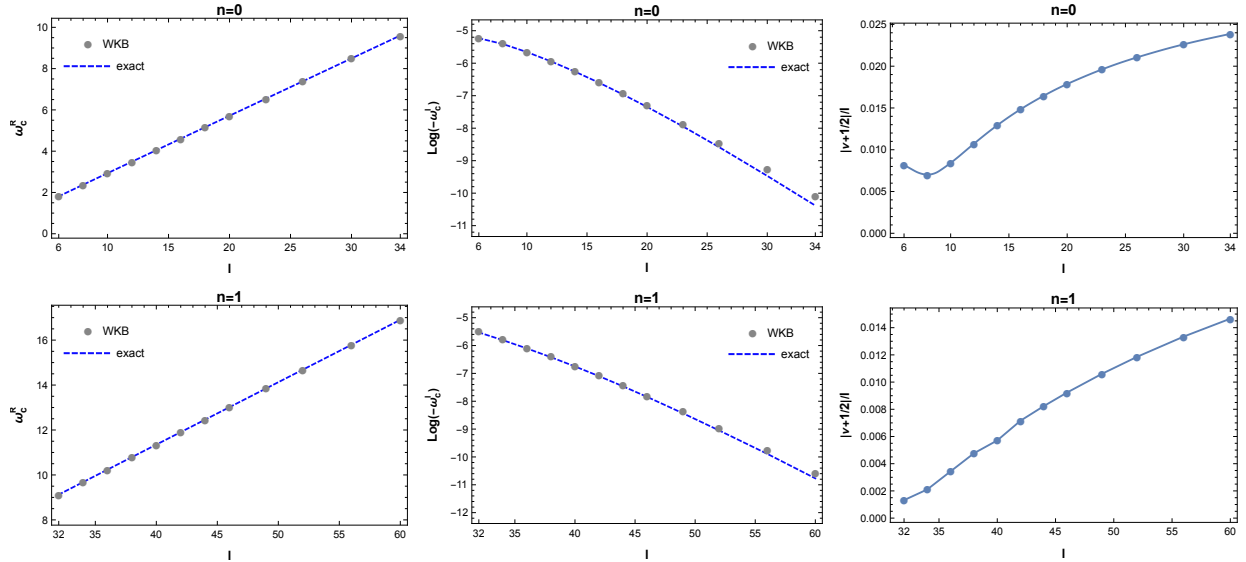


FIG. 4. Real part (**Left**), imaginary part (**Middle**) and  $|\nu + 1/2|/l$  (**Right**) of the quasinormal modes, which are trapped at the local maximum of the effective potential, for the branches of  $n = 0$  (**Upper**) and  $n = 1$  (**Lower**). The left column shows that the real parts of the WKB results (gray dots) agree well with these of exact modes (blue dashed lines). In the middle column, the imaginary parts of WKB and exact results match well for small  $l$ , and start to deviate from each other when  $l$  becomes larger. As shown in the right column, the value of  $|\nu + 1/2|/l$  grows as  $l$  increases, which means that the WKB approximation may not be accurate for a large  $l$ .

Since the distance between  $x_3$  and  $x_4$  is assumed to be small, the value of  $\nu + 1/2$  should be tiny compared to  $l$ . In fact, the matching condition (34) is valid to evaluate quasinormal modes when the condition  $|\nu + 1/2| \ll l$  is satisfied [85]. Note that the valley of the effective potential becomes deeper/shallower as  $l$  increases/decreases. For a given  $n$ , a large  $l$  would drive the  $(\omega_c^2)^R$  line away from the local maximum at  $x = x_c$ , thus making the first term in the left-hand side of eqn. (34) small enough to satisfy eqn. (34). However, if  $(\omega_c^2)^R$  is not close enough to the local maximum, the condition  $|\nu + 1/2| \ll l$  can be violated, which indicates that the WKB result (34) is not a good approximation when  $l$  is too large. In the case with large  $l$ , the effective potential can be approximated by a linear function near the turning points  $x_3$  and  $x_4$ , which leads to the WKB results (31) and (32). For an even larger  $l$ , the  $(\omega_c^2)^R$  line can lie close to the minimum of the potential, which corresponds to the aforementioned long-lived modes at low excitations. On the other hand, when  $l$  decreases, the first term in the left-hand side of eqn. (34) requires that the  $(\omega_c^2)^R$  line moves toward the local maximum when  $n$  is fixed. Interestingly, a too small  $l$  can make

		exact Modes	WKB Modes	$2\pi(n - n^*)/I$
$n = 0$	$l = 5$	$\pm 1.5308 - 0.00556i$	$\pm 1.5323 - 0.00479i$	0.0006
	$l = 6$	$\pm 1.8135 - 0.00535i$	$\pm 1.8148 - 0.00463i$	-0.0010
$n = 1$	$l = 31$	$\pm 8.8483 - 0.00453i$	$\pm 8.8486 - 0.00421i$	0.0257
	$l = 32$	$\pm 9.1263 - 0.00397i$	$\pm 9.1267 - 0.00372i$	-0.0033
$n = 2$	$l = 54$	$\pm 15.3090 - 0.00402i$	$\pm 15.3092 - 0.00381i$	0.0145
	$l = 55$	$\pm 15.5871 - 0.00353i$	$\pm 15.5874 - 0.00336i$	-0.0135
$n = 3$	$l = 76$	$\pm 21.4905 - 0.00406i$	$\pm 21.4906 - 0.00385i$	0.0256
	$l = 77$	$\pm 21.7686 - 0.00359i$	$\pm 21.7688 - 0.00343i$	-0.0016
$n = 4$	$l = 99$	$\pm 27.9497 - 0.00365i$	$\pm 27.9498 - 0.00349i$	0.0080
	$l = 100$	$\pm 28.2278 - 0.00323i$	$\pm 28.2281 - 0.00309i$	-0.0186
$n = 5$	$l = 121$	$\pm 34.1306 - 0.00371i$	$\pm 34.1307 - 0.00355i$	0.0165
	$l = 122$	$\pm 34.4088 - 0.00330i$	$\pm 34.4089 - 0.00317i$	-0.0096

TABLE I. Pairs of sub-long-lived modes for different values of  $n$ . These quasinormal modes are evaluated near the local maximum of the effective potential, corresponding to an unstable circular null geodesic. The exact modes are numerically obtained using a direct integration, which can be approximated well by the WKB method for small magnitude of  $2\pi(n - n^*)/I$ .

$(\omega_c^2)^R$  greater than the local maximum, hence rendering the turning points  $x_3$  and  $x_4$  unable to exist. So the WKB result (34) may cease to exist when  $l$  is too small.

In FIG. 4, two branches of quasinormal modes are obtained using eqns. (34) and (35), i.e.,  $n = 0$  in the upper row and  $n = 1$  in the lower row. Moreover, we also plot the value of  $|\nu + 1/2|/l$  as a function of  $l$  for each branch of the quasinormal modes in the right column, which checks the validity of the WKB approximation. Compared with exact modes (blue dashed lines), the real part of the quasinormal modes (gray dots) is well approximated by the WKB method. By contrast, the imaginary part of the WKB result matches that of exact modes well except when  $l$  is too large, for which, as displayed in the right column, the condition  $|\nu + 1/2| \ll l$  is not well satisfied. It also shows that there exists a lowest  $l$  for each branch (e.g.,  $l = 6$  for  $n = 0$  and  $l = 32$  for  $n = 1$ ), below which the WKB results do not exist. Note that the exact modes of  $n = 0$  presented in FIGs. 3 and 4 are precisely the same. As expected, the exact modes are accurately described by the WKB results (34) and (26) for small and large  $l$ , respectively.

To find the relation between the quasinormal modes and the parameters of circular null geodesics, we focus on the limit  $|\nu + 1/2| \ll 1$ . In this limit, the matching condition (34) is

further simplified (see Appendix A for the derivation),

$$\begin{aligned} (\omega_c^2)^R &\approx V_l(x_c) + \frac{\sqrt{-2V_l^{(2)}(x_c)}2\pi I}{I^2 + \pi^2/4} \left( n - n^* - \frac{e^{-2\int_{x_1}^{x_2} \sqrt{V_l(x) - \omega_c^2} dx}}{8I} \right), \\ (\omega_c^2)^I &\approx -\frac{\log 2}{2I} \sqrt{-2V_l^{(2)}(x_c)} - \frac{\sqrt{-2V_l^{(2)}(x_c)}\pi^2}{I^2 + \pi^2/4} \left( n - n^* - \frac{I e^{-2\int_{x_1}^{x_2} \sqrt{V_l(x) - \omega_c^2} dx}}{2\pi^2} \right), \end{aligned} \quad (36)$$

where  $I$  is

$$I = \log \left( \sqrt{-2V_l^{(2)}(x_c)} (x_c - x_2)^2 \right) + 2 \int_{x_2}^{x_c} \left( \frac{\sqrt{-2V_l^{(2)}(x_c)}}{2\sqrt{V_l(x_c) - V_l(x)}} - \frac{1}{(x_c - x)} \right) dx + (\gamma + \log 2\pi), \quad (37)$$

with a constant  $\gamma = 0.5772$ . Here, the number  $n^*$  is defined as

$$n^* \equiv \frac{1}{\pi} \int_{x_2}^{x_c} \sqrt{V_l(x_c) - V_l(x)} dx + \frac{\log 2}{8I} - \frac{1}{2}, \quad (38)$$

which can be interpreted as the number of a resonance filling the potential well until  $(\omega_c^2)^R = V_l(x_c)$  in the eikonal limit. Moreover, the condition  $|\nu + 1/2| \ll 1$  requires

$$\frac{2\pi|n - n^*|}{I} \ll 1, \quad (39)$$

which provides a constraint on  $n$  and  $l$ . For quasinormal modes of given  $n$ , there appears to exist a pair of adjacent integers  $l$  that well satisfy the constraint (39). For  $n \leq 5$ , TABLE. I displays the quasinormal modes with such adjacent  $l$ . In this case, it shows that the exact (obtained by a numerical direct integration method) and WKB (obtained from eqn. (36)) results agree well with each other.

When  $n$  is large enough, the value of  $l$  satisfying the constraint (39) can be arbitrarily large. In the large  $l$  limit, eqn. (36) reduces to

$$\begin{aligned} \omega_c^R &\sim l \sqrt{V_{\text{geo}}(x_c)} = \Omega_c l, \\ \omega_c^I &\sim -\frac{\log 2}{2 \log l} \lambda_c, \end{aligned} \quad (40)$$

where we use  $I \sim \log l$  for  $l \gg 1$ . Here  $\Omega_c$  is the angular velocity of the unstable circular null geodesic at  $x = x_c$ , and  $\lambda_c$  is the corresponding Lyapunov exponent. For these quasinormal modes, the turning points  $x_3$  and  $x_4$  are very close to  $x_c$ , and hence their real part  $\omega_c^R$  is proportional to the angular velocity  $\Omega_c$ . Similar to the global maximum case, the Lyapunov exponent of the outer unstable circular orbit contributes to the imaginary part of the quasinormal modes. However, these quasinormal modes can temporarily trap in the potential valley, which gives a logarithmically decaying factor  $1/\log l$  in their imaginary part. For this reason, this type of quasinormal modes is dubbed as sub-long-lived modes.

#### IV. CONCLUSIONS

In this paper, we studied quasinormal modes of a scalar field in hairy black hole spacetime, where the scalar field is minimally coupled to the gravity sector and non-minimally coupled to the electromagnetic field with an exponential coupling function. Intriguingly, the hairy black holes have been demonstrated to possess two unstable and one stable circular null geodesics on the equatorial plane outside the event horizon, corresponding to two maxima and one minimum of the geometric potential for null geodesic motion, respectively. It showed that, apart from a constant prefactor, the effective potential governing quasinormal modes of the scalar perturbation can be well approximated by the geometric potential in the eikonal regime. To explore the relation between quasinormal modes and the parameters of the circular null geodesics, we used the WKB method to compute quasinormal modes living near the global maximum, the smaller local maximum and the minimum of the effective potential.

In the large  $l$  limit, the real part of these quasinormal modes was shown to be proportional to the angular velocity of the corresponding circular null geodesics, which implies that the quasinormal modes can be related to particles traveling along the circular null geodesics. However, since the imaginary part  $\omega_I$  describes the perturbation decay timescale,  $\omega_I$  was found to have distinct behaviors, depending on the location of the quasinormal modes. For the quasinormal modes near the global maximum,  $\omega_I$  can be interpreted as slowly leaking out of particles trapped at the unstable circular null geodesics, and is related to the Lyapunov exponent, which reflects the instability timescale of geodesic motion. On the other hand, the effective potential valley between two maxima plays a key role in determining the behavior of  $\omega_I$  of quasinormal modes near the local maximum and the minimum in the eikonal regime. When  $l \gg 1$ , the depth of the potential valley was found to be proportional to  $l^2$ . The quasinormal modes living at the bottom of the potential valley (i.e., the minimum) are metastable states with tunneling out through the high potential barriers, which gives that  $\omega_I$  decays exponentially with respect to  $l$ . There appeared to be two contributions to  $\omega_I$  of the quasinormal modes near the local maximum, i.e., classical leaking out from the unstable circular null geodesics, which makes  $\omega_I$  proportional to the Lyapunov exponent, and tunneling out through the global maximum barrier, which makes  $\omega_I$  inversely proportional to  $\log l$ . Due to the exponential and logarithmic suppressions in  $\omega_I$ , the quasinormal modes in the neighborhoods of the minimum and local maximum can live for a long time, and hence were dubbed as long-lived and sub-long-lived modes, respectively.

The long-lived modes may accumulate along the stable circular orbit, and eventually develop

a non-linear instability. Moreover for a spinning object, the existence of long-lived modes may also trigger an ergoregion instability at the linear level in the static limit [42]. These instabilities imply that long-lived modes trapped at the stable circular orbit could destabilize the background spacetime by their backreaction. In the future studies, it is of great interest to further address the instabilities of long-lived and sub-long-lived modes in a hairy black hole, and explore the end point of a hairy black hole possessing three circular null geodesics in a dynamic evolution.

### ACKNOWLEDGMENTS

We are grateful to Yiqian Chen and Qingyu Gan for useful discussions and valuable comments. This work is supported in part by NSFC (Grant No. 12105191, 11947225 and 11875196). Houwen Wu is supported by the International Visiting Program for Excellent Young Scholars of Sichuan University.

### Appendix A: Derivations of Eqns. (34) and (36)

In this appendix, we follow [84–86] to give derivations of eqns. (34) and (36). As presented in FIG. 2, we consider the  $(\omega_c^2)^R$  line close to the local maximum at  $x = x_c$ , and discuss the WKB solutions in different ranges of  $x$ . When  $x_2 < x < x_3$ , the WKB solution is

$$\Psi_{\text{I}}(x) \sim [\omega_c^2 - V_l(x)]^{-1/4} \sin \left( \int_{x_2}^x \sqrt{\omega_c^2 - V_l(x')} dx' + \frac{\pi}{4} + \frac{i}{4} e^{-2 \int_{x_1}^{x_2} \sqrt{V_l(x) - \omega_c^2} dx} \right). \quad (\text{A1})$$

For  $x > x_4$ , the outgoing WKB solution is

$$\Psi_{\text{III}}(x) \sim [\omega_c^2 - V_l(x)]^{-1/4} e^{i \int_{x_4}^x \sqrt{\omega_c^2 - V_l(x')} dx'}. \quad (\text{A2})$$

In the interval  $(x_-, x_+)$ , the effective potential is approximated by a parabolic expansion, for which the perturbative equation (20) can be exactly solved. To match the WKB solution (A2) in the region  $(x_4, x_+)$ , the exact solution  $\Psi_{\text{II}}(x)$  is then given by

$$\Psi_{\text{II}}(x) \sim D_\nu(t), \quad (\text{A3})$$

where  $D_\nu(t)$  represents the parabolic cylinder function,  $\nu$  is defined in eqn. (35), and  $t \equiv e^{i\pi/4} [-2V_l^{(2)}(x_c)]^{1/4} (x - x_c)$ . On the other hand, to match the solution (A3) with the exact solution  $\Psi_{\text{II}}(x)$  in the region  $(x_-, x_3)$ , the WKB solution for  $x_2 < x < x_3$  should be

$$\Psi_{\text{I}}'(x) \sim [\omega_c^2 - V_l(x)]^{-1/4} \sin \left( \int_x^{x_3} \sqrt{\omega_c^2 - V_l(x')} dx' + \xi + \frac{\pi}{2} \right), \quad (\text{A4})$$

where  $\xi$  is defined in eqn. (35). To satisfy  $\Psi_I(x) \propto \Psi'_I(x)$  for  $x \in (x_2, x_3)$ , the sum of the components of sine functions in eqns. (A1) and (A4) must be a multiple of  $\pi$ , which gives eqn. (34).

In the limit  $|\nu + 1/2| \ll 1$ , the first term of the left-hand side of eqn. (34) becomes

$$\begin{aligned} \int_{x_2}^{x_3} \sqrt{\omega_c^2 - V_l(x)} dx &= \int_{x_2}^{x_-} \sqrt{\omega_c^2 - V_l(x)} dx + \int_{x_-}^{x_3} \sqrt{\omega_c^2 - V_l(x)} dx \\ &\approx \int_{x_2}^{x_c} \sqrt{V_l(x_c) - V_l(x)} dx + \frac{ia}{2} \left( \log(ia) - 1 - \log \left[ \sqrt{-2V_l^{(2)}(x_c)} (x_c - x_2)^2 \right] \right) \\ &\quad - ia \int_{x_2}^{x_c} \left( \frac{\sqrt{-2V_l^{(2)}(x_c)}}{2\sqrt{V_l(x_c) - V_l(x)}} - \frac{1}{(x_c - x)} \right) dx. \end{aligned} \quad (\text{A5})$$

where we replace the effective potential by a parabola in the region  $(x_-, x_c)$ , and  $a = \nu + 1/2$ . Moreover,  $\xi$  in eqn. (34) can be expanded as

$$\xi \approx \frac{i}{2} \left( -i\pi a - a \ln a + \frac{\ln 2}{2} + \frac{i\pi}{2} + a [1 - (\gamma + \ln 2 + \ln \pi)] \right), \quad (\text{A6})$$

where  $\gamma = 0.5772$ . From eqns. (34), (A5) and (A6), one can extract the real and imaginary parts of  $\omega_c^2$ , which gives eqn. (36).

- 
- [1] B.P. Abbott et al. Observation of Gravitational Waves from a Binary Black Hole Merger. *Phys. Rev. Lett.*, 116(6):061102, 2016. [arXiv:1602.03837](https://arxiv.org/abs/1602.03837), [doi:10.1103/PhysRevLett.116.061102](https://doi.org/10.1103/PhysRevLett.116.061102). I
  - [2] Kazunori Akiyama et al. First M87 Event Horizon Telescope Results. I. The Shadow of the Supermassive Black Hole. *Astrophys. J. Lett.*, 875:L1, 2019. [arXiv:1906.11238](https://arxiv.org/abs/1906.11238), [doi:10.3847/2041-8213/ab0ec7](https://doi.org/10.3847/2041-8213/ab0ec7). I
  - [3] Kazunori Akiyama et al. First M87 Event Horizon Telescope Results. II. Array and Instrumentation. *Astrophys. J. Lett.*, 875(1):L2, 2019. [arXiv:1906.11239](https://arxiv.org/abs/1906.11239), [doi:10.3847/2041-8213/ab0c96](https://doi.org/10.3847/2041-8213/ab0c96).
  - [4] Kazunori Akiyama et al. First M87 Event Horizon Telescope Results. III. Data Processing and Calibration. *Astrophys. J. Lett.*, 875(1):L3, 2019. [arXiv:1906.11240](https://arxiv.org/abs/1906.11240), [doi:10.3847/2041-8213/ab0c57](https://doi.org/10.3847/2041-8213/ab0c57).
  - [5] Kazunori Akiyama et al. First M87 Event Horizon Telescope Results. IV. Imaging the Central Supermassive Black Hole. *Astrophys. J. Lett.*, 875(1):L4, 2019. [arXiv:1906.11241](https://arxiv.org/abs/1906.11241), [doi:10.3847/2041-8213/ab0e85](https://doi.org/10.3847/2041-8213/ab0e85).
  - [6] Kazunori Akiyama et al. First M87 Event Horizon Telescope Results. V. Physical Origin of the Asymmetric Ring. *Astrophys. J. Lett.*, 875(1):L5, 2019. [arXiv:1906.11242](https://arxiv.org/abs/1906.11242), [doi:10.3847/2041-8213/ab0f43](https://doi.org/10.3847/2041-8213/ab0f43).
  - [7] Kazunori Akiyama et al. First M87 Event Horizon Telescope Results. VI. The Shadow and Mass of the Central Black Hole. *Astrophys. J. Lett.*, 875(1):L6, 2019. [arXiv:1906.11243](https://arxiv.org/abs/1906.11243), [doi:10.3847/2041-8213/ab1141](https://doi.org/10.3847/2041-8213/ab1141). I

- [8] Emanuele Berti, Vitor Cardoso, Jose A. Gonzalez, and Ulrich Sperhake. Mining information from binary black hole mergers: A Comparison of estimation methods for complex exponentials in noise. *Phys. Rev. D*, 75:124017, 2007. [arXiv:gr-qc/0701086](#), [doi:10.1103/PhysRevD.75.124017](#). I
- [9] Valeria Ferrari and Bahram Mashhoon. New approach to the quasinormal modes of a black hole. *Phys. Rev. D*, 30:295–304, 1984. [doi:10.1103/PhysRevD.30.295](#). I
- [10] Hans-Peter Nollert. TOPICAL REVIEW: Quasinormal modes: the characteristic ‘sound’ of black holes and neutron stars. *Class. Quant. Grav.*, 16:R159–R216, 1999. [doi:10.1088/0264-9381/16/12/201](#). I
- [11] Gary T. Horowitz and Veronika E. Hubeny. Quasinormal modes of AdS black holes and the approach to thermal equilibrium. *Phys. Rev. D*, 62:024027, 2000. [arXiv:hep-th/9909056](#), [doi:10.1103/PhysRevD.62.024027](#).
- [12] E. Berti and K. D. Kokkotas. Quasinormal modes of Reissner-Nordström-anti-de Sitter black holes: Scalar, electromagnetic and gravitational perturbations. *Phys. Rev. D*, 67:064020, 2003. [arXiv:gr-qc/0301052](#), [doi:10.1103/PhysRevD.67.064020](#).
- [13] Yun Soo Myung, Yong-Wan Kim, and Young-Jai Park. Quasinormal modes from potentials surrounding the charged dilaton black hole. *Eur. Phys. J. C*, 58:617–625, 2008. [arXiv:0809.1933](#), [doi:10.1140/epjc/s10052-008-0802-4](#).
- [14] Emanuele Berti, Vitor Cardoso, and Andrei O. Starinets. Quasinormal modes of black holes and black branes. *Class. Quant. Grav.*, 26:163001, 2009. [arXiv:0905.2975](#), [doi:10.1088/0264-9381/26/16/163001](#).
- [15] R. A. Konoplya and A. Zhidenko. Quasinormal modes of black holes: From astrophysics to string theory. *Rev. Mod. Phys.*, 83:793–836, 2011. [arXiv:1102.4014](#), [doi:10.1103/RevModPhys.83.793](#).
- [16] Huan Yang, David A. Nichols, Fan Zhang, Aaron Zimmerman, Zhongyang Zhang, and Yanbei Chen. Quasinormal-mode spectrum of Kerr black holes and its geometric interpretation. *Phys. Rev. D*, 86:104006, 2012. [arXiv:1207.4253](#), [doi:10.1103/PhysRevD.86.104006](#). I
- [17] Gregory B. Cook and Maxim Zaltuskiy. Purely imaginary quasinormal modes of the Kerr geometry. *Class. Quant. Grav.*, 33(24):245008, 2016. [arXiv:1603.09710](#), [doi:10.1088/0264-9381/33/24/245008](#).
- [18] Yun Soo Myung and De-Cheng Zou. Quasinormal modes of scalarized black holes in the Einstein–Maxwell–Scalar theory. *Phys. Lett. B*, 790:400–407, 2019. [arXiv:1812.03604](#), [doi:10.1016/j.physletb.2019.01.046](#).
- [19] R. A. Konoplya, A. Zhidenko, and A. F. Zinhailo. Higher order WKB formula for quasinormal modes and grey-body factors: recipes for quick and accurate calculations. *Class. Quant. Grav.*, 36:155002, 2019. [arXiv:1904.10333](#), [doi:10.1088/1361-6382/ab2e25](#).
- [20] Jose Luis Blázquez-Salcedo, Carlos A.R. Herdeiro, Sarah Kahlen, Jutta Kunz, Alexandre M. Pombo, and Eugen Radu. Quasinormal modes of hot, cold and bald Einstein-Maxwell-scalar black holes. 8 2020. [arXiv:2008.11744](#). I
- [21] Daniela D. Doneva, Stoytcho S. Yazadjiev, Kostas D. Kokkotas, and Ivan Zh. Stefanov. Quasi-normal

- modes, bifurcations and non-uniqueness of charged scalar-tensor black holes. *Phys. Rev. D*, 82:064030, 2010. [arXiv:1007.1767](#), [doi:10.1103/PhysRevD.82.064030](#). I
- [22] Jose Luis Blázquez-Salcedo, Daniela D. Doneva, Jutta Kunz, and Stoytcho S. Yazadjiev. Radial perturbations of the scalarized Einstein-Gauss-Bonnet black holes. *Phys. Rev. D*, 98(8):084011, 2018. [arXiv:1805.05755](#), [doi:10.1103/PhysRevD.98.084011](#).
- [23] Yun Soo Myung and De-Cheng Zou. Instability of Reissner–Nordström black hole in Einstein-Maxwell-scalar theory. *Eur. Phys. J. C*, 79(3):273, 2019. [arXiv:1808.02609](#), [doi:10.1140/epjc/s10052-019-6792-6](#). I
- [24] Yun Soo Myung and De-Cheng Zou. Stability of scalarized charged black holes in the Einstein–Maxwell–Scalar theory. *Eur. Phys. J. C*, 79(8):641, 2019. [arXiv:1904.09864](#), [doi:10.1140/epjc/s10052-019-7176-7](#). I, III
- [25] De-Cheng Zou and Yun Soo Myung. Radial perturbations of the scalarized black holes in Einstein-Maxwell-conformally coupled scalar theory. *Phys. Rev. D*, 102(6):064011, 2020. [arXiv:2005.06677](#), [doi:10.1103/PhysRevD.102.064011](#). I
- [26] Guangzhou Guo, Peng Wang, Houwen Wu, and Haitang Yang. Scalarized Einstein–Maxwell-scalar black holes in anti-de Sitter spacetime. *Eur. Phys. J. C*, 81(10):864, 2021. [arXiv:2102.04015](#), [doi:10.1140/epjc/s10052-021-09614-7](#). I, II A
- [27] Vitor Cardoso, João L. Costa, Kyriakos Destounis, Peter Hintz, and Aron Jansen. Quasinormal modes and Strong Cosmic Censorship. *Phys. Rev. Lett.*, 120(3):031103, 2018. [arXiv:1711.10502](#), [doi:10.1103/PhysRevLett.120.031103](#). I
- [28] Qingyu Gan, Guangzhou Guo, Peng Wang, and Houwen Wu. Strong cosmic censorship for a scalar field in a Born-Infeld–de Sitter black hole. *Phys. Rev. D*, 100(12):124009, 2019. [arXiv:1907.04466](#), [doi:10.1103/PhysRevD.100.124009](#).
- [29] Qingyu Gan, Peng Wang, Houwen Wu, and Haitang Yang. Strong Cosmic Censorship for a Scalar Field in an Einstein-Maxwell-Gauss-Bonnet-de Sitter Black Hole. *Chin. Phys. C*, 45(2):025103, 2021. [arXiv:1911.10996](#), [doi:10.1088/1674-1137/abccaf](#). I
- [30] Jose P. S. Lemos and Oleg B. Zaslavskii. Black hole mimickers: Regular versus singular behavior. *Phys. Rev. D*, 78:024040, 2008. [arXiv:0806.0845](#), [doi:10.1103/PhysRevD.78.024040](#). I
- [31] Pedro V. P. Cunha, José A. Font, Carlos Herdeiro, Eugen Radu, Nicolas Sanchis-Gual, and Miguel Zilhão. Lensing and dynamics of ultracompact bosonic stars. *Phys. Rev. D*, 96(10):104040, 2017. [arXiv:1709.06118](#), [doi:10.1103/PhysRevD.96.104040](#).
- [32] Pedro V. P. Cunha and Carlos A. R. Herdeiro. Shadows and strong gravitational lensing: a brief review. *Gen. Rel. Grav.*, 50(4):42, 2018. [arXiv:1801.00860](#), [doi:10.1007/s10714-018-2361-9](#).
- [33] Rajibul Shaikh, Pritam Banerjee, Suvankar Paul, and Tapobrata Sarkar. A novel gravitational lensing feature by wormholes. *Phys. Lett. B*, 789:270–275, 2019. [Erratum: *Phys.Lett.B* 791, 422–423 (2019)]. [arXiv:1811.08245](#), [doi:10.1016/j.physletb.2018.12.030](#).
- [34] Hyat Huang and Jinbo Yang. Charged Ellis Wormhole and Black Bounce. *Phys. Rev. D*, 100(12):124063,

2019. [arXiv:1909.04603](#), [doi:10.1103/PhysRevD.100.124063](#).
- [35] Maciek Wielgus, Jiri Horak, Frederic Vincent, and Marek Abramowicz. Reflection-asymmetric wormholes and their double shadows. *Phys. Rev. D*, 102(8):084044, 2020. [arXiv:2008.10130](#), [doi:10.1103/PhysRevD.102.084044](#).
- [36] Jinbo Yang and Hyat Huang. Trapping horizons of the evolving charged wormhole and black bounce. *Phys. Rev. D*, 104(8):084005, 2021. [arXiv:2104.11134](#), [doi:10.1103/PhysRevD.104.084005](#).
- [37] Jun Peng, Minyong Guo, and Xing-Hui Feng. Observational Signature and Additional Photon Rings of Asymmetric Thin-shell Wormhole. 2 2021. [arXiv:2102.05488](#). I
- [38] Zachary Mark, Aaron Zimmerman, Song Ming Du, and Yanbei Chen. A recipe for echoes from exotic compact objects. *Phys. Rev. D*, 96(8):084002, 2017. [arXiv:1706.06155](#), [doi:10.1103/PhysRevD.96.084002](#). I
- [39] Pablo Bueno, Pablo A. Cano, Frederik Goelen, Thomas Hertog, and Bert Vercknocke. Echoes of Kerr-like wormholes. *Phys. Rev. D*, 97(2):024040, 2018. [arXiv:1711.00391](#), [doi:10.1103/PhysRevD.97.024040](#).
- [40] Vitor Cardoso and Paolo Pani. Testing the nature of dark compact objects: a status report. *Living Rev. Rel.*, 22(1):4, 2019. [arXiv:1904.05363](#), [doi:10.1007/s41114-019-0020-4](#).
- [41] Min-Yan Ou, Meng-Yun Lai, and Hyat Huang. Echoes from Asymmetric Wormholes and Black Bounce. 11 2021. [arXiv:2111.13890](#). I
- [42] Vitor Cardoso, Luís C. B. Crispino, Caio F. B. Macedo, Hirotada Okawa, and Paolo Pani. Light rings as observational evidence for event horizons: long-lived modes, ergoregions and nonlinear instabilities of ultracompact objects. *Phys. Rev. D*, 90(4):044069, 2014. [arXiv:1406.5510](#), [doi:10.1103/PhysRevD.90.044069](#). I, IIIB, IIIB, IV
- [43] Joe Keir. Slowly decaying waves on spherically symmetric spacetimes and ultracompact neutron stars. *Class. Quant. Grav.*, 33(13):135009, 2016. [arXiv:1404.7036](#), [doi:10.1088/0264-9381/33/13/135009](#).
- [44] Minyong Guo, Zhen Zhong, Jinguang Wang, and Sijie Gao. Light rings and long-lived modes in quasi-black hole spacetimes. 8 2021. [arXiv:2108.08967](#). I, IIIB
- [45] John L. Friedman. Ergosphere instability. *Communications in Mathematical Physics*, 63:243–255, 1978. I
- [46] Cecilia B. M. H. Chirenti and Luciano Rezzolla. On the ergoregion instability in rotating gravastars. *Phys. Rev. D*, 78:084011, 2008. [arXiv:0808.4080](#), [doi:10.1103/PhysRevD.78.084011](#).
- [47] Paolo Pani, Vitor Cardoso, Mariano Cadoni, and Marco Cavaglia. Ergoregion instability of black hole mimickers. *PoS, BHGRS:027*, 2008. [arXiv:0901.0850](#), [doi:10.22323/1.075.0027](#). I
- [48] Vitor Cardoso, Alex S. Miranda, Emanuele Berti, Helvi Witek, and Vilson T. Zanchin. Geodesic stability, Lyapunov exponents and quasinormal modes. *Phys. Rev. D*, 79:064016, 2009. [arXiv:0812.1806](#), [doi:10.1103/PhysRevD.79.064016](#). I, IIC, IIC, IIC, IIC, IIIA
- [49] R. A. Konoplya and Z. Stuchlík. Are eikonal quasinormal modes linked to the unstable circular null

- geodesics? *Phys. Lett. B*, 771:597–602, 2017. [arXiv:1705.05928](#), [doi:10.1016/j.physletb.2017.06.015](#).
- [50] Kimet Jusufi. Quasinormal Modes of Black Holes Surrounded by Dark Matter and Their Connection with the Shadow Radius. *Phys. Rev. D*, 101(8):084055, 2020. [arXiv:1912.13320](#), [doi:10.1103/PhysRevD.101.084055](#).
- [51] B. Cuadros-Melgar, R. D. B. Fontana, and Jeferson de Oliveira. Analytical correspondence between shadow radius and black hole quasinormal frequencies. *Phys. Lett. B*, 811:135966, 2020. [arXiv:2005.09761](#), [doi:10.1016/j.physletb.2020.135966](#).
- [52] Wei-Liang Qian, Kai Lin, Xiao-Mei Kuang, Bin Wang, and Rui-Hong Yue. Quasinormal modes in two-photon autocorrelation and the geometric-optics approximation. 9 2021. [arXiv:2109.02844](#). I
- [53] Werner Israel. Event horizons in static vacuum space-times. *Phys. Rev.*, 164:1776–1779, 1967. [doi:10.1103/PhysRev.164.1776](#). I
- [54] B. Carter. Axisymmetric Black Hole Has Only Two Degrees of Freedom. *Phys. Rev. Lett.*, 26:331–333, 1971. [doi:10.1103/PhysRevLett.26.331](#).
- [55] Remo Ruffini and John A. Wheeler. Introducing the black hole. *Phys. Today*, 24(1):30, 1971. [doi:10.1063/1.3022513](#). I
- [56] M.S. Volkov and D.V. Galtsov. NonAbelian Einstein Yang-Mills black holes. *JETP Lett.*, 50:346–350, 1989. I
- [57] P. Bizon. Colored black holes. *Phys. Rev. Lett.*, 64:2844–2847, 1990. [doi:10.1103/PhysRevLett.64.2844](#).
- [58] Brian R. Greene, Samir D. Mathur, and Christopher M. O’Neill. Eluding the no hair conjecture: Black holes in spontaneously broken gauge theories. *Phys. Rev. D*, 47:2242–2259, 1993. [arXiv:hep-th/9211007](#), [doi:10.1103/PhysRevD.47.2242](#).
- [59] Hugh Luckock and Ian Moss. BLACK HOLES HAVE SKYRMION HAIR. *Phys. Lett. B*, 176:341–345, 1986. [doi:10.1016/0370-2693\(86\)90175-9](#).
- [60] Serge Droz, Markus Heusler, and Norbert Straumann. New black hole solutions with hair. *Phys. Lett. B*, 268:371–376, 1991. [doi:10.1016/0370-2693\(91\)91592-J](#).
- [61] P. Kanti, N.E. Mavromatos, J. Rizos, K. Tamvakis, and E. Winstanley. Dilatonic black holes in higher curvature string gravity. *Phys. Rev. D*, 54:5049–5058, 1996. [arXiv:hep-th/9511071](#), [doi:10.1103/PhysRevD.54.5049](#).
- [62] Subhash Mahapatra, Supragyan Priyadarshinee, Gosala Narasimha Reddy, and Bhaskar Shukla. Exact topological charged hairy black holes in AdS Space in  $D$ -dimensions. *Phys. Rev. D*, 102(2):024042, 2020. [arXiv:2004.00921](#), [doi:10.1103/PhysRevD.102.024042](#). I
- [63] Carlos A.R. Herdeiro, Eugen Radu, Nicolas Sanchis-Gual, and José A. Font. Spontaneous Scalarization of Charged Black Holes. *Phys. Rev. Lett.*, 121(10):101102, 2018. [arXiv:1806.05190](#), [doi:10.1103/PhysRevLett.121.101102](#). I, II A
- [64] D. Astefanesei, C. Herdeiro, A. Pombo, and E. Radu. Einstein-Maxwell-scalar black holes: classes of so-

- lutions, dyons and extremality. *JHEP*, 10:078, 2019. [arXiv:1905.08304](#), [doi:10.1007/JHEP10\(2019\)078](#).
- [65] Pedro G.S. Fernandes, Carlos A.R. Herdeiro, Alexandre M. Pombo, Eugen Radu, and Nicolas Sanchis-Gual. Charged black holes with axionic-type couplings: Classes of solutions and dynamical scalarization. *Phys. Rev. D*, 100(8):084045, 2019. [arXiv:1908.00037](#), [doi:10.1103/PhysRevD.100.084045](#).
- [66] Pedro G. S. Fernandes, Carlos A. R. Herdeiro, Alexandre M. Pombo, Eugen Radu, and Nicolas Sanchis-Gual. Spontaneous Scalarisation of Charged Black Holes: Coupling Dependence and Dynamical Features. *Class. Quant. Grav.*, 36(13):134002, 2019. [Erratum: *Class.Quant.Grav.* 37, 049501 (2020)]. [arXiv:1902.05079](#), [doi:10.1088/1361-6382/ab23a1](#).
- [67] Yan Peng. Scalarization of horizonless reflecting stars: neutral scalar fields non-minimally coupled to Maxwell fields. *Phys. Lett. B*, 804:135372, 2020. [arXiv:1912.11989](#), [doi:10.1016/j.physletb.2020.135372](#).
- [68] De-Cheng Zou and Yun Soo Myung. Scalarized charged black holes with scalar mass term. *Phys. Rev. D*, 100(12):124055, 2019. [arXiv:1909.11859](#), [doi:10.1103/PhysRevD.100.124055](#).
- [69] Dumitru Astefanesei, Carlos Herdeiro, João Oliveira, and Eugen Radu. Higher dimensional black hole scalarization. *JHEP*, 09:186, 2020. [arXiv:2007.04153](#), [doi:10.1007/JHEP09\(2020\)186](#).
- [70] Jose Luis Blázquez-Salcedo, Carlos A.R. Herdeiro, Jutta Kunz, Alexandre M. Pombo, and Eugen Radu. Einstein-Maxwell-scalar black holes: the hot, the cold and the bald. *Phys. Lett. B*, 806:135493, 2020. [arXiv:2002.00963](#), [doi:10.1016/j.physletb.2020.135493](#).
- [71] Pedro G.S. Fernandes. Einstein-Maxwell-scalar black holes with massive and self-interacting scalar hair. *Phys. Dark Univ.*, 30:100716, 2020. [arXiv:2003.01045](#), [doi:10.1016/j.dark.2020.100716](#).
- [72] Hong Guo, Xiao-Mei Kuang, Eleftherios Papantonopoulos, and Bin Wang. Topology and spacetime structure influences on black hole scalarization. 12 2020. [arXiv:2012.11844](#).
- [73] Yun Soo Myung and De-Cheng Zou. Scalarized charged black holes in the Einstein-Maxwell-Scalar theory with two U(1) fields. *Phys. Lett. B*, 811:135905, 2020. [arXiv:2009.05193](#), [doi:10.1016/j.physletb.2020.135905](#).
- [74] Yun Soo Myung and De-Cheng Zou. Scalarized black holes in the Einstein-Maxwell-scalar theory with a quasitopological term. *Phys. Rev. D*, 103(2):024010, 2021. [arXiv:2011.09665](#), [doi:10.1103/PhysRevD.103.024010](#).
- [75] Peng Wang, Houwen Wu, and Haitang Yang. Scalarized Einstein-Born-Infeld-scalar Black Holes. 12 2020. [arXiv:2012.01066](#).
- [76] Qingyu Gan, Peng Wang, Houwen Wu, and Haitang Yang. Photon spheres and spherical accretion image of a hairy black hole. *Phys. Rev. D*, 104(2):024003, 2021. [arXiv:2104.08703](#), [doi:10.1103/PhysRevD.104.024003](#). I
- [77] Qingyu Gan, Peng Wang, Houwen Wu, and Haitang Yang. Photon ring and observational appearance of a hairy black hole. *Phys. Rev. D*, 104(4):044049, 2021. [arXiv:2105.11770](#), [doi:10.1103/PhysRevD.104.044049](#). I

- [78] Guangzhou Guo, Peng Wang, Houwen Wu, and Haitang Yang. Thermodynamics and Phase Structure of an Einstein-Maxwell-scalar Model in Extended Phase Space. 7 2021. [arXiv:2107.04467](#). I
- [79] Yun Soo Myung and De-Cheng Zou. Onset of rotating scalarized black holes in Einstein-Chern-Simons-Scalar theory. *Phys. Lett. B*, 814:136081, 2021. [arXiv:2012.02375](#), [doi:10.1016/j.physletb.2021.136081](#). I
- [80] Hai-Shan Liu, Zhan-Feng Mai, Yue-Zhou Li, and H. Lü. Quasi-topological Electromagnetism: Dark Energy, Dyonic Black Holes, Stable Photon Spheres and Hidden Electromagnetic Duality. *Sci. China Phys. Mech. Astron.*, 63:240411, 2020. [arXiv:1907.10876](#), [doi:10.1007/s11433-019-1446-1](#). I
- [81] Yves Brihaye and Betti Hartmann. Boson stars and black holes with wavy scalar hair. 12 2021. [arXiv:2112.12830](#).
- [82] Hyat Huang, Min-Yan Ou, Meng-Yun Lai, and H. Lu. Echoes from Classical Black Holes. 12 2021. [arXiv:2112.14780](#). I
- [83] Neil J. Cornish and Janna J. Levin. Lyapunov timescales and black hole binaries. *Class. Quant. Grav.*, 20:1649–1660, 2003. [arXiv:gr-qc/0304056](#), [doi:10.1088/0264-9381/20/9/304](#). II C
- [84] Bernard F. Schutz and Clifford M. Will. BLACK HOLE NORMAL MODES: A SEMIANALYTIC APPROACH. *Astrophys. J. Lett.*, 291:L33–L36, 1985. [doi:10.1086/184453](#). III A, A
- [85] Boris Mikhailovich Karnakov and Vladimir Pavlovich Krainov. *WKB Approximation in Atomic Physics*. Springer Berlin Heidelberg, 2013. [doi:10.1007/978-3-642-31558-9](#). III B, III B, III C
- [86] Carl M. Bender and Steven A. Orszag. *Advanced Mathematical Methods for Scientists and Engineers I*. Springer New York, 1999. [doi:10.1007/978-1-4757-3069-2](#). III B, A